Multibody Syst Dyn (2010) 23: 333–360
DOI 10.1007/s11044-010-9188-9

A cohesive modeling technique for theoretical and experimental estimation of damping in serial robots with rigid and flexible links

Ashish Mohan · S.P. Singh · S.K. Saha

Received: 24 September 2008 / Accepted: 15 January 2010 / Published online: 5 February 2010

Abstract Dynamic model incorporating damping characteristics, namely joint damping and structural damping in flexible links, of the serial robots with rigid and flexible links is presented. A novel procedure, based on the unified approach of theoretical formulation and analysis of experimental data, is proposed for the estimation of damping coefficients. First, the dynamic model of a robotic system with rigid and flexible links is presented. Next, the modifications in the dynamic model due to the considerations of damping characteristics of joints and structural damping characteristics of the flexible links are presented. A systematic methodology based on analysis of data obtained from experiments is presented for estimation and determination of damping coefficients of rigid-flexible links. The determination of joint damping coefficients, is based on the logarithmic decay of the amplitude of the oscillations of robotic links, while the structural damping coefficients are estimated mainly using the modal analysis and the method of evolving spectra. The method of evolving spectra, based on the Fast Fourier Transform of the decay of the amplitude in structural vibrations of the robot links in progressive windows is used to estimate the structural damping ratios while the critical structural coefficients are determined using the modal analysis. The methodology is illustrated through a series of simple experiments on simple robotic systems. The experimental results are then compared with the simulation results incorporating the damping coefficients determined using the proposed procedure. The comparisons leads to the validation of the proposed dynamic modeling technique, modeling of the damping characteristics, and the method proposed for estimation of damping coefficients for rigid-flexible link robotic systems.

Keywords Rigid-flexible · Dynamic modeling · Damping-joint and structural · Estimation techniques · Experiments · Logarithmic decay · Water-fall method

The work reported in this paper was carried out in the Dept. of Mechanical Engineering, Indian Institute of Technology Delhi, New Delhi 110016, India.

A. Mohan (✉)
Product Engg. Dept., JCB India Ltd., Faridabad, India
e-mail: ashish.mohan13@gmail.com

S.P. Singh · S.K. Saha
Dept. of Mechanical Engg., Indian Institute of Technology Delhi, New Delhi, India

1 Introduction

Dynamics of flexible link manipulators is highly nonlinear, configuration dependent, and computationally complex. Moreover, real robotic systems always involve external factors such as joint damping, structural damping in the flexible links, working environment of the robot, etc., which cannot be modeled without reasonable assumptions. As a result, the dynamic equations of the rigid-flexible robots, like the ones presented in [1–4], represent only idealized and approximate models of the actual systems. Attempts by various researchers [5–7] to theoretically estimate the damping factors of a system have been only partially successful. Consequently, experiments have generally been conducted by the different researchers to quantify the above physical parameters which cannot be easily modeled in the dynamic equations. Thus, Mingli et al. [8] have conducted experiments on a two flexible-link arm to identify the damping characteristics in the motion and overall friction coming on the robot. Chapnik et al. [9] have experimentally investigated the projectile impact dynamics of an unactuated flexible beam. Feliu et al. [10] have conducted the experiments on a three degree of freedom robot to control its position using sensors and feedback loops. Mavroidis et al. [11] and Stieber et al. [12] have conducted experiments on the multilink robot whose end effector is supported on a long and flexible link. Similarly, De Luca and Siciliano [13] have used the experimental results to study the regulation of the flexible arms under gravity. Similarly, Bragliato [14], Queiroz et al. [15], and Feliu et al. [16] have validated the dynamic models proposed by them using experimental verifications, and extended the results for feedback control. Different experimental methodologies adopted by the above researchers vary mainly in its approaches, e.g., the type of sensors to measure vibrations, architecture of the robot, initial conditions, etc., and make trade-offs amongst the contradicting requirements. For example, while the frequency of rotational joint oscillations is moderate, the frequency of the vibrations of the flexible link is very high; hence it is difficult to experimentally measure both the parameters using a single sensor. Consequently, various researchers have adopted different combination of sensors, data acquisition systems, and actuators to study the tip performance characteristics. Also, note that a study conducted under open-loop control provides a better scenario for simulation validation since the use of feedback ends to mask some of the flexibility effects present in the system [17]. Moreover, the inclusion of damping in the dynamic model also improves the numerical stability characteristics [4, 18] of the simulation algorithm [1, 19].

It is clear from the above that the study of damping, its estimation, and incorporation into the real robotic systems is an area of research and has wide interest. Note that a robotic system has damping mainly because of two reasons: (1) due to friction at the joint assembly, namely joint damping; and (2) due to structural stiffness of its links, namely structural damping, which manifest itself physically in the form of decay in the amplitude of vibrations of the link. In this paper, a cohesive technique for the dynamic modeling of rigid-flexible link robots incorporating the effects of damping is presented and a novel procedure, based on the unified approach of theoretical formulation and analysis of experimental data, is proposed for the estimation of damping coefficients. The overall objectives of the experiments conducted are (i) to incorporate damping into the model, and (ii) to validate the theoretical model. The experimental procedure presented in this paper for the determination of joint damping coefficients, is based on the logarithmic decay of the amplitude of the oscillations of robotic links. The structural damping coefficients are estimated using a novel approach based upon the modal analysis [20] and the method of evolving spectra [21]. First, the effects of damping in different modes of vibrations are decoupled using the modal analysis. The method of evolving spectra, also called the Waterfall method, is then proposed in the paper to determine the structural damping coefficients using the Fast Fourier transform of the vibration response on the flexible in progressive time windows. The method is illustrated using a single rigid link, single flexible link, and a two-flexible links robotic arm. Comparisons of the experimental results with the simulation results for both the free and forced responses are presented. The results of the experiments are complemented with the theoretical models to estimate more accurate behavior of the robotic systems.

The paper is organized as follows: After a brief Introduction and overview of the related work done by various researchers in Sect. 1, the dynamic equations of rigid-flexible robotic systems incorporating damping characteristics of rigid/flexible links are presented in Sect. 2. Next, the methodology and procedures proposed for estimation of damping coefficients, joint, and structural, are presented in Sect. 3. The method of determination of joint damping coefficients is illustrated using a single rigid link in Sect. 3.1.1. The method for determination of structural damping coefficients using modal analysis and method of evolving spectra is presented in Sect. 3.2 and illustrated using a cantilever type flexible link, clamped at one end and undergoing natural vibrations in Sect. 3.3. Building upon the above, example of a single flexible link with revolute joint and falling freely under gravity is presented as a simple representative of robotic systems with both joint and structural damping in Sect. 4.1 Finally, the overall application of the proposed methodology and procedure to estimate damping characteristics is presented on an experimental setup of two flexible links robotic arm, which is considered as a simple representative of coupled flexible links systems as well as serial robotic systems in Sect. 4.2. Details of experimental set-up and comparison of experimental and simulation results are also presented. Conclusions are presented in Sect. 5.

2 Dynamic model of serial robots with rigid-flexible links with damping

In this section, the dynamic model of the serial robotic systems with rigid and flexible links with damping is presented. The inclusion of damping factors into the dynamic model is important for any realistic simulation and meaningful comparison of the simulation results with the experimental ones. While damping in a rigid robotic system results mainly due to joint assembly, damping in a flexible link is of two types: joint damping and structural damping. The decay in the amplitude of the oscillations of a link is due to friction at its joint, which is referred to as joint damping, whereas decay in the amplitude of vibrations of a flexible link is due to its structural stiffness, which is called as structural damping. Both the types of damping characteristics are directly proportional to the first derivative (rate) of the associated generalized coordinates [22]. For a rigid link, structural damping is absent as the generalized coordinates associated with the vibrations of the link does not exist. Figure 1a shows a serial robotic system having a fixed base and n rigid-flexible moving bodies. The flexible part is assumed to vibrate in space due to bending in m_i modes and due to torsion in $\bar{m}_i$ modes, respectively. Hence, the degrees of freedom of the rigid-flexible serial robot are $\bar{n} \equiv n + \sum_{i=1}^{n_f}(3m_i + \bar{m}_i)$, where $n \equiv n_r + n_f$ is the total number of links or joints in which n_r is the number of rigid links and n_f is the number of flexible links. Figure 1b shows an i^{th} link of the robotic chain. Now,

(1) Using the Decoupled Natural Orthogonal Complement (DeNOC) matrices for flexible links as derived in [4] and [19], the dynamic equations of motion for the rigid-flexible robots can be written as

$$\boldsymbol{N}_d^T \boldsymbol{N}_l^T (\boldsymbol{M}\dot{\boldsymbol{t}} + \gamma) = \tau \tag{1}$$

where $\boldsymbol{M}$ is the $\hat{n} \times \hat{n}$ generalized mass matrix, $\boldsymbol{t}$ is the $\hat{n}$-dimensional generalized twist of the robotic system as defined in [19]. Moreover, the $\hat{n}$-dimensional vectors, $\boldsymbol{t}$ and γ,

Fig. 1a A n-sink serial robot

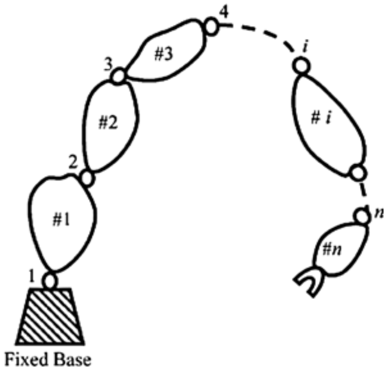

Fig. 1b Position of elemental link, dx_i on i^{th} flexible link

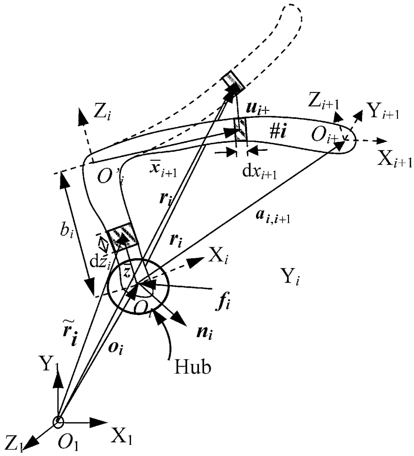

are respectively the generalized twist and generalized inertia wrench as defined in [19]. Furthermore, τ, is the $\bar{n}$-dimensional vector of generalized forces/torque [19]. Note that $\hat{n} \equiv 6n_r + (6 + 3m_i + \bar{m}_i)n_f$ and, $\boldsymbol{N}_l$ and $\boldsymbol{N}_d$, are respectively the $(6 + 3m + \bar{m}_i) \times (6 + 3m_i + \bar{m}_i)n$ lower block triangular and the $\bar{n} \times \bar{n}$ block diagonal DeNOC matrices for the flexible robot at hand which are defined as follows:

$$N_l \equiv \begin{bmatrix} \mathbf{1} & \boldsymbol{O} & \cdots & \boldsymbol{O} \\ \boldsymbol{A}_{21} & \mathbf{1} & \cdots & \boldsymbol{O} \\ \vdots & \vdots & \ddots & \\ \boldsymbol{A}_{n1} & \boldsymbol{A}_{n2} & \cdots & \mathbf{1} \end{bmatrix}; \qquad \boldsymbol{N}_d \equiv \begin{bmatrix} \boldsymbol{P}_1 & \mathbf{0} & \cdots & \mathbf{0} \\ \mathbf{0} & \boldsymbol{P}_2 & \cdots & \mathbf{0} \\ \vdots & \vdots & \ddots & \\ \mathbf{0} & \mathbf{0} & \cdots & \boldsymbol{P}_n \end{bmatrix} \tag{2}$$

in which $\boldsymbol{A}_{i,i-1}$ is the $(6 + 3m + \bar{m}_i) \times (6 + 3m_i + \bar{m}_i)$ twist propagation matrix and $\boldsymbol{P}_i$ is the $(6 + 3m + \bar{m}_i) \times (6 + 3m_i + \bar{m}_i)$ flexible motion propagation matrix [19].

(2) Note that $\boldsymbol{t} = \boldsymbol{N}_l \boldsymbol{N}_d \dot{\boldsymbol{q}}$, in which $\dot{\boldsymbol{q}}_i$ is the $\bar{n}$ dimensional vector of rates of joint-and-amplitude vector of time-rate of change of the joint-and-amplitude vector of the i^{th} flexible link given by $\boldsymbol{q}_i \equiv [\theta_i \ \boldsymbol{d}_i^T \ \boldsymbol{c}_i^T\ ]^T$: where θ_i is the rotational or translational displacement of the i^{th} joint depending on its type, i.e., revolute or prismatic, respectively [4, 19]. Moreover, $\boldsymbol{d}_i$ is the $3m_i$-dimensional vector of the time dependent amplitudes due to bending vibrations and $\bar{m}_i$-dimensional vectors, $\boldsymbol{c}_i$, are the torsional time-dependent amplitudes.

(3) Thus, substituting, $\dot{\boldsymbol{t}} = \boldsymbol{N}_l\boldsymbol{N}_d\ddot{\boldsymbol{q}} + \boldsymbol{N}_l\dot{\boldsymbol{N}}_d\dot{\boldsymbol{q}} + \dot{\boldsymbol{N}}_l\boldsymbol{N}_d\dot{\boldsymbol{q}}$ into (1), the dynamic equations of motion of the rigid-flexible robot are obtained as [4, 19]

$$\boldsymbol{I}\ddot{\boldsymbol{q}} = \boldsymbol{\phi} \tag{3}$$

where the elements of the generalized inertia matrix $\boldsymbol{I}$ are $(1+3m_i+\bar{m}_i)\times(1+3m_i+\bar{m}_i)$ block matrices that are represented as

$$\boldsymbol{I}_{ij} = \boldsymbol{I}_{ji}^T = \boldsymbol{P}_i^T\tilde{\boldsymbol{M}}_i\boldsymbol{A}_{ij}\boldsymbol{P}_j; \quad \text{for } i=1,\ldots,n;\ j=1,\ldots,i \tag{4a}$$

and the $(1+3m_i+\bar{m}_i)\times(1+3m_i+\bar{m}_i)$ matrix, $\tilde{\boldsymbol{M}}_i$, is obtained recursively as

$$\tilde{\boldsymbol{M}}_i \equiv \boldsymbol{M}_i + \boldsymbol{A}_{i+1,i}^T\tilde{\boldsymbol{M}}_{i+1}\boldsymbol{A}_{i,i+1}; \qquad \tilde{\boldsymbol{M}}_{n+1} \equiv \boldsymbol{O}, \tag{4b}$$

as there is no $(n+1)^{\text{st}}$ link in the chain.

(4) Note that (3) represents the dynamic equations of an undamped system. Now, considering the damping in the system, (3) is modified as

$$\boldsymbol{I}\ddot{\boldsymbol{q}} = \boldsymbol{\phi} + \boldsymbol{Z}\dot{\boldsymbol{q}} \tag{5}$$

where $\bar{n}$-dimensional vector of joint rates $\dot{\boldsymbol{q}}$ and the $(1+3m_i+\bar{m}_i)$-dimensional vectors of joint-and-amplitudes, $\dot{q}_i$, are defined in (2). The $\bar{n}\times\bar{n}$ damping coefficient matrix, $\boldsymbol{Z}$, is accordingly represented as

$$\mathrm{Z} = \begin{bmatrix} \boldsymbol{Z}_1 & \cdots & \boldsymbol{O} \\ \vdots & \ddots & \\ \boldsymbol{O} & & \boldsymbol{Z}_n \end{bmatrix} \tag{6a}$$

where $\boldsymbol{Z}_i$, for $i=1,\ldots,n$, is the $(1+3m_i+\bar{m}_i)$-dimensional matrix given by

$$\mathrm{Z}_i = \begin{bmatrix} \kappa_i & \mathbf{0} \\ \mathbf{0} & \zeta_i \end{bmatrix} \tag{6b}$$

in which the scalar κ_i represents the damping coefficient at the joint and the $m_i\times m_i$-dimensional diagonal matrix, ζ_i, corresponds to the structural damping of vibration of the link in $\boldsymbol{m}_i$ modes in bending. Moreover, for rigid links the damping coefficient matrix associated with link, i, namely $\boldsymbol{Z}_i$, reduce to scalar κ_i. The joint damping coefficient κ_i and the elements of structural damping coefficients matrix ζ_i are determined here from the experimental data. The methodologies adopted for the determination of the joint damping and structural damping coefficients are presented next.

3 Estimation of damping coefficients

In this section, methodologies to determine the joint and structural damping coefficients are presented.

3.1 Joint damping

Friction in mechanical contacts is influenced by many parameters, including the properties of contact surfaces, the running conditions, and any lubricants used. For the oscillating sliding joints in the experiments presented in this paper, various models, namely, Coulomb friction model and logarithmic decay, viscous friction model and Stribeck friction model, have been proposed in the literature to model the joint friction [23, 24]. In mechanical oscillating joints with little lubrication, the Coulomb friction model and logarithmic decay models are often used [24]. However, since the equation of motion for dynamic systems is strongly nonlinear with a logarithmic decay model, a viscous friction model is also used [23]. Viscous friction model, on the other hand, gives rise to inaccurate final position in simulations with small applied forces or if the friction force is supposed to hold a load over a longer time. In literature concerning joint friction of (lubricated) bearings, often so-called Stribeck models are used [24]. The Stribeck friction model can provide very good representation of the friction between sliding surfaces and sliding friction in lubricated contacts running under boundary, mixed, and full film conditions. It covers everything from Coulomb friction to viscous friction, depending on the choice of parameter values. However, the Stribeck friction model presents the same problem as the viscous friction model when it comes to changing sliding direction where the friction value is dependent on the applied force and the contact surfaces are sticking to each other [23]. Accordingly, a combined Stribeck and viscous model accommodating the transition to pure sliding in either direction is reported in literature [25]. However, the main disadvantage of the Coulomb and Stribeck friction models is the undetermined friction force at zerosliding speed. These friction models run into problems at the start of a motion and at the point where the motion reverses. Although the behavior at these points can be modeled by a sign function, which represents the behavior fairly well, the representation complicates simulations and necessitates extra condition checks of the system states or interruptions of the simulations. Various tricks can be used to overcome the problem, such as replacing the sign function with a viscous saturated function, or using a tanh function. These modifications improve the ability of friction models to simulate the behavior of systems, but do not represent small displacements very well [23]. Another disadvantage of the Coulomb and Stribeck model is that the model does not adequately describe the viscous friction behavior for the full velocity range in the sliding regime [26]. Jonker et al. [26] have shown that friction models incorporating Coulomb, (linear) viscous and Stribeck components are inadequate to describe the friction behavior for the full velocity range.

There are other friction models also for the incorporation of microslip in friction models, namely, Dankowicz model and Dahl friction model [23, 24]. The derived model is, however, rather complex to use in other simulation tools, for the displacements have to be set equal to zero at turning points [23]. Hence, while the elastic Coulomb friction and logarithmic decay model represents the reality only reasonably well, it simplifies the numerical calculations and is mostly used by researchers to model the joint friction in robotic systems [27–30]. Moreover, in servodrives and the dry lubrication regiems, the joint amplitude decay is generally modeled using logarithmic decay model [24]. The logarithmic decrement in the free-decay process, evaluated from the continuous change in amplitude during free decay, differs remarkably from that in the steady-state vibration, and thus reflects the dislocation motion more sensitively [27] Furthermore, the method is quick and applicable over a wide range of energy dissipating systems [29]. In addition, the logarithmic decay model makes it possible to integrate and interface the model into the total system model without extra condition checks on the state of the system or interruptions in the model.

Hence, in this paper, joint damping coefficients are measured using the logarithmic decay model characteristics.

The joint damping coefficient, κ_i, for a robotic system is given by

$$\kappa_i = \xi_i \bar{\kappa}_i \tag{7a}$$

where ξ_i is the joint damping ratio and $\bar{\kappa}_i$ is the joint critical damping factor associated with the i^{th} joint [22]. Using the logarithmic decay, the joint damping ratio, ξ_i, is determined by measuring the rate of logarithmic decay (logarithmic) of the oscillations of the link and is given by

$$\xi_i = \frac{1}{2\pi(k-1)} \log_e\left(\frac{x_1}{x_k}\right) \tag{7b}$$

in which x_i and x_p are respectively the amplitudes in 1^{st} and k^{th} cycles of the oscillation of the link. The critical damping factor associated with the i^{th} joint, $\bar{\kappa}_i$, is obtained as

$$\bar{\kappa}_i = 4\pi \rho_i a_i \eta_f \tag{7c}$$

where ρ_i is the mass per unit length, a_i is the length—one of the four DH-parameters [19]—and η_f is the natural frequency of oscillation of the i^{th} link.

3.1.1 An illustration: a single rigid link

The method of determination of the joint damping coefficient, κ_i, as presented above, is now illustrated using an example of a single rigid link falling freely under gravity. The only scalar equation of motion represented in the form of (5) is given by

$$\left(\frac{\rho a^3}{3} + I_h\right)\ddot{\theta} = \tau + \kappa\dot{\theta} \tag{8}$$

where ρ, a, θ, I_h and τ are respectively the mass per unit length, link length, joint angle, inertia due to the hub at the root of link, and the external torque due to gravity, whereas κ is the associated joint damping coefficient of the system that will be determined from the experimental data and using (7a)–(7c). The scheme of the experiment conducted is shown in Fig. 2. The physical parameters of the link and the set-up are shown in Table 1. The angular displacement of the link is measured using the wire-pot potentiometer, 2 of Fig. 2, mounted at the joint. The link is allowed to fall freely under gravity from an initial angular displacement of 7 deg from vertical. The initial displacement is kept small to keep the joint oscillations small, so that nonlinear behavior of the damping coefficients is minimized. The corresponding angular displacement of the link, as measured by the potentiometer, is shown in Fig. 3. The amplitudes of the 1^{st} and 2^{nd} oscillations are x_1 and x_2, as indicated in Fig. 3. The ratio of the successive amplitudes of oscillations is obtained from it and used in (7b) to obtain the damping ratio, $\xi_1 = 0.0142$, whereas the critical damping factor associated with the joint, namely, $\bar{\kappa}_1$, is obtained from (7c) using the physical parameters of the link given in Table 1(a) and its natural frequency, η_f, as obtained from the experimental results. The value of $\bar{\kappa}_1 = 2.1716$ kg/s. The joint damping coefficient, κ_1, is then obtained from (7a) as 0.0308 kg/s for the single rigid link under study. The joint damping coefficient, κ_1, is next incorporated into (8) and the simulation for the same initial conditions is repeated. The resulting angular variation is plotted in Fig. 3 and compared with those obtained from the experiments. It is seen that the experimental and simulation results match closely, thus

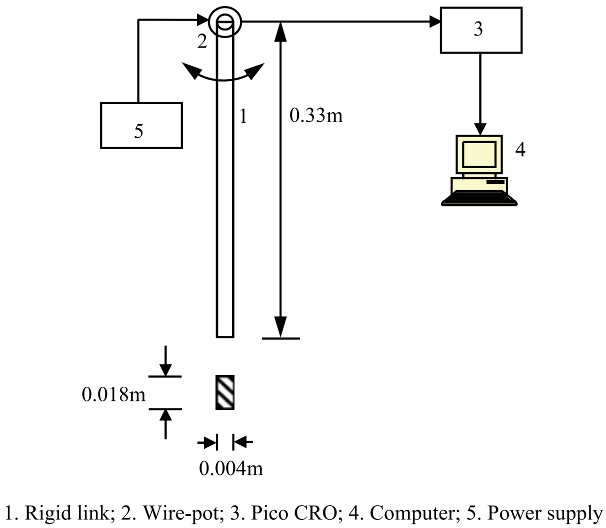

Fig. 2 Experimental set-up for the single rigid link

Table 1 Experiment with single rigid link (Fig. 2)

(a) Physical parameters of the link, 1

Material	Length, *a* (m)	Cross-section (m^2)	Mass (kg)	Mass/length, ρ (kg/m)	Hub inertia (kg m^2)
Carbon steel	0.33	0.018×0.004	0.180	0.5455	2.95×10^{-5}

(b) Specifications of the equipments

Equipment	Specifications
Potentiometer, 2	10 kΩ, ±0.25% linearity, wire-wound pot
Data acquisition system, 3 and 4	PICO CRO with Pentium IV Intel processor computer
Power supply, 5	Regulated 5 V, 1 A, DC

verifying the modeling technique of the joint damping in the dynamic model. The frequency of oscillation is also obtained from the Fourier transform of the experimental response for the joint angles. This is obtained as 0.96 Hz, while the frequency of oscillation of the link, as obtained from the simulation results is 1.0 Hz, which is a good match. The difference in the experimental and simulation results is, however, slightly increasing in the latter part. This is mainly because in (8) it is assumed that the decay due to the joint damping is linear and the higher order terms are neglected. In reality, the decay curve is hyperbolic [22] and remains linear during the initial cycles only. Modeling the hyperbolic decay of oscillation amplitudes is quite complex, and hence for illustration purposes, a linear model is implemented which provided fairly accurate results as discussed above in Sect. 3.1 before (7a).

3.2 Structural damping

The vibration amplitude of a flexible link is a combination of several modes. In order to determine the structural damping, it is required to separate out the decay in amplitudes of

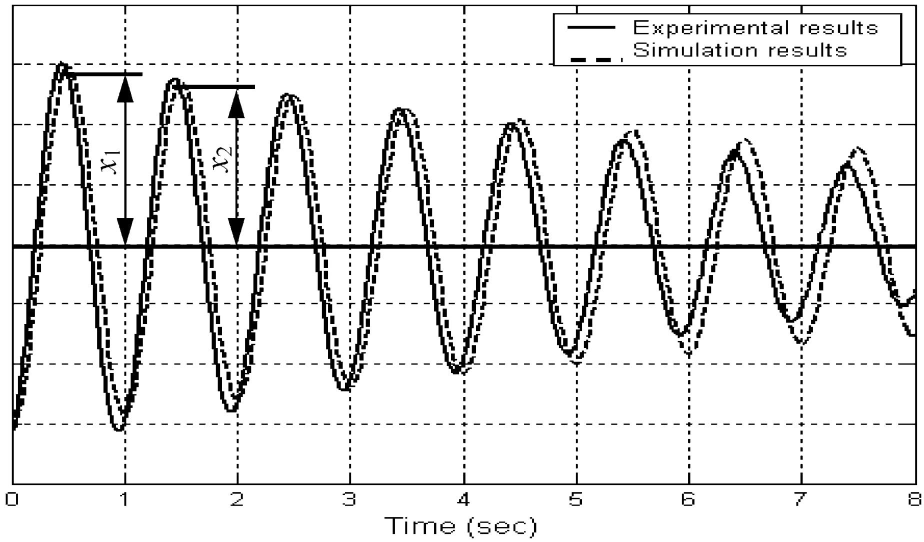

Fig. 3 Experimental and simulation results for a single rigid link

vibration due to each mode. This decoupling is essential because the structural damping coefficient of a beam is different in each of its mode. For a beam, vibrating in m_i modes of vibrations in bending, and $\bar{m}_i$ modes of vibrations in torsion, the associated structural damping coefficients are given by the diagonal elements of the $(m_i + \bar{m}_i) \times (m_i + \bar{m}_i)$ diagonal matrix, ζ_i of (6b). Similar to the joint damping, (7a) the matrix, ζ_i, for structural damping coefficients is defined as

$$\zeta_i = \tilde{\xi}_i \bar{\zeta}_i \tag{9a}$$

where $\tilde{\xi}_i$ is the $(m_i + \bar{m}_i) \times (m_i + \bar{m}_i)$-dimensional diagonal matrix of damping ratios associated with the m_i modes of vibrations in bending and $\bar{m}_i$ modes in torsion, of the i^{th} link, and $\bar{\zeta}_i$ is the $(m_i + \bar{m}_i) \times (m_i + \bar{m}_i)$-dimensional matrix of critical damping factors associated with the respective modes. The matrices $\tilde{\xi}_i$ and $\bar{\zeta}_i$ are thus defined as

$$\tilde{\xi}_i = \begin{bmatrix} \tilde{\xi}_{i1} & \cdots & & 0 \\ \vdots & \ddots & & \\ \vdots & & \tilde{\xi}_{ij} & \\ 0 & & & \tilde{\xi}_{iC} \end{bmatrix}, \qquad \bar{\zeta}_i = \begin{bmatrix} \bar{\zeta}_{i1} & \cdots & & 0 \\ \vdots & \ddots & & \\ \vdots & & \bar{\zeta}_{ij} & \\ 0 & & & \bar{\zeta}_{iC} \end{bmatrix} \tag{9b}$$

where $\tilde{\xi}_{ij}$, for $j = 1, \ldots, m_i$, is the damping ratio of the i^{th} link in its j^{th} mode, referred here as the modal damping ratio, and $\tilde{\xi}_{iC}$ is the $\bar{m}_i \times \bar{m}_i$ damping ratio matrix associated with the vibration of the i^{th} link in torsion. In order to isolate the decay in the amplitude of vibration of link in each mode and to determine the corresponding damping ratios $\tilde{\xi}_{ij}$, the method of evolving spectra [21] is adopted here, whereas the critical damping factor, $\bar{\zeta}_{ij}$, for $j = 1, \ldots, m_i$, is obtained from the modal analysis of the link [22]. In this paper, for the comparison of experimental and simulation results, the torsional vibration is neglected due to the types of beams selected in the experimental set-up. Hence, the damping ratio matrix, $\tilde{\xi}_{iC}$, vanishes.

3.2.1 Method of evolving spectra

The method, also referred as the Waterfall method [21], is based on the sequential Fast Fourier Transform (FFT) performed on amplitude response of the vibrating links in progressive time window. First, the amplitude response of the vibrating link is recorded in a selected time window. The Fast Fourier transform (FFT) of the response in this time window is then performed. The natural frequencies of the link, known in advance from a real time analyzer, are identified as the sharp peaks in the FFT response. Thus, the corresponding amplitude of the link vibration in each mode is obtained. The time window is then shifted forward and FFT of the response in the shifted time window is performed again. The amplitude corresponding to each mode is then noted for this shifted position of time window. The process is repeated several times, depending upon the level of accuracy desired in the simulation, by shifting the time window progressively. The amplitudes of the FFT curves corresponding to a particular mode in each time window are then plotted. It is found that the decay curve for the amplitudes corresponding to a mode is logarithmic, which provides the damping ratio as

$$\tilde{\xi}_{ij} = \frac{1}{2\pi \eta_j \Delta t_k} \log_e\left(\frac{x_{j1}}{x_{jk}}\right) \tag{9c}$$

where η_j is the natural frequency of vibration of i^{th} link in its j^{th} mode, and x_{j1} and x_{jk} are the amplitudes of the vibrations in the 1^{st} and k^{th} time windows of the response. Moreover, Δt_k is the shift in time for the k^{th} time window with respect to the first time window. Alternatively, the amplitude decay of the peaks of the FFT curves for the $1^{\text{st}}, \ldots, k^{\text{th}}$ natural frequencies are plotted against time on a semi-logarithmic scale. The slope of the curve divided by the corresponding natural frequency of the mode gives the structural damping ratio for the particular mode at hand. These steps will be further illustrated in Sect. 3.3.

3.2.2 Critical damping

The matrix of critical damping factors, $\bar{\zeta}_i$ of (9b), is obtained by the modal analysis of the link [22], which is given by

$$\bar{\zeta}_i = 2\sqrt{\tilde{K}_{di}\tilde{M}_{di}} \tag{10a}$$

where the $(m_i + \bar{m}_i) \times (m_i + \bar{m}_i)$-dimensional diagonal matrices, $\tilde{K}_{di}$ and $\tilde{M}_{di}$, are respectively the modal stiffness and modal mass matrices of the i^{th} link. For a link vibrating in space in all three directions, namely, X, Y, and Z, in m_i modes in bending only, $\tilde{K}_{di}$ and $\tilde{M}_{di}$ are the $(3m_i + \bar{m}_i) \times (3m_i + \bar{m}_i)$ matrices, which can be written using the modal analysis as

$$\tilde{\boldsymbol{K}}_{di} \equiv \int_0^{a_i} E_i I_i \begin{bmatrix} \bar{\boldsymbol{S}}_i^x & & & \\ & \bar{\boldsymbol{S}}_i^y & & \\ & & \bar{\boldsymbol{S}}_i^z & \\ & & & \boldsymbol{O}_{\bar{m}_i} \end{bmatrix}^{\mathrm{T}} \begin{bmatrix} \bar{\boldsymbol{S}}_i^x & & & \\ & \bar{\boldsymbol{S}}_i^y & & \\ & & \bar{\boldsymbol{S}}_i^z & \\ & & & \boldsymbol{O}_{\bar{m}_i} \end{bmatrix} \mathrm{d}\bar{a}_{i+1} \tag{10b}$$

$$\tilde{\boldsymbol{M}}_{di} \equiv \int_0^{a_i} \rho_i \begin{bmatrix} \boldsymbol{S}_i^x & & & \\ & \boldsymbol{S}_i^y & & \\ & & \boldsymbol{S}_i^z & \\ & & & \boldsymbol{O}_{\bar{m}_i} \end{bmatrix} \begin{bmatrix} \boldsymbol{S}_i^x & & & \\ & \boldsymbol{S}_i^y & & \\ & & \boldsymbol{S}_i^z & \\ & & & \boldsymbol{O}_{\bar{m}_i} \end{bmatrix} \mathrm{d}\bar{a}_{i+1} \tag{10c}$$

Fig. 4 Determination of structural damping coefficients

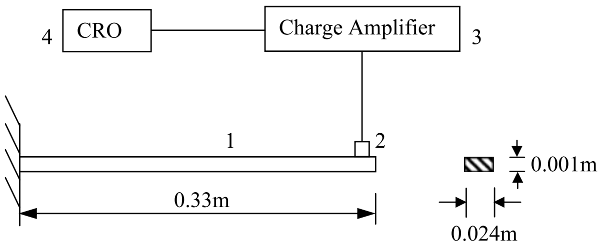

where $E_i I_i$ and ρ_i are respectively the flexure stiffness and mass per unit length of the i^{th} link, and $\boldsymbol{O}_{\bar{m}_i}$ is the $\bar{m}_i \times \bar{m}_i$ zero matrix due to the absence of torsional vibration. However, the $m_i \times m_i$-dimensional matrices, $\bar{\boldsymbol{S}}_i^x$, $\bar{\boldsymbol{S}}_i^y$ and $\bar{\boldsymbol{S}}_i^z$; and $\boldsymbol{S}_i^x$, $\boldsymbol{S}_i^y$, and $\boldsymbol{S}_i^z$, are the matrices associated with the shape functions for the vibrations about $\hat{X}_{i+1}$-, $\hat{Y}_{i+1}$- and $\hat{Z}_{i+1}$- axis, respectively. Thus,

$$\bar{\boldsymbol{S}}_i^x \equiv \begin{bmatrix} \frac{\partial s_{i,1}^x}{\partial \bar{a}_i} & & \boldsymbol{O} \\ & \ddots & \\ \boldsymbol{O} & & \frac{\partial s_{i,m_i}^x}{\partial \bar{a}_i} \end{bmatrix}; \qquad \boldsymbol{S}_i^x \equiv \begin{bmatrix} s_{i,1}^x & & \boldsymbol{O} \\ & \ddots & \\ \boldsymbol{O} & & s_{i,m_i}^x \end{bmatrix} \tag{10d}$$

where for, $j = 1, \ldots, m_i$, $s_{i,j}^x$ is the shape function for the link in its j^{th} mode. The $m_i \times m_i$-dimensional matrices $\boldsymbol{S}_i^y$, $\boldsymbol{S}_i^z$, $\bar{\boldsymbol{S}}_i^y$, and $\bar{\boldsymbol{S}}_i^z$ are defined similarly for the shape functions associated with vibrations about $\hat{Y}_{i+1}$ and $\hat{Z}_{i+1}$-axes. Since it is difficult to apply appropriate control with complete accuracy, the vibrations in all the dimensions of a link of a robot in the laboratory environment, the geometry of the link are purposefully selected so that they have significant vibrations only in bending and in the plane perpendicular to the joints. The geometry of the beams selected is rectangular with very large slenderness ratio so as to provide maximum flexibility in the plane perpendicular to the joint axis. Thus, being insignificant in comparison to vibrations about joint axis only, the vibrations about $\hat{X}_{i+1}$, $\hat{Y}_{i+1}$-axes are neglected, i.e., the matrices, $\boldsymbol{S}_i^x$, $\boldsymbol{S}_i^y$, $\bar{\boldsymbol{S}}_i^x$, and $\bar{\boldsymbol{S}}_i^y$ vanish, and $\tilde{\boldsymbol{K}}_{di}$ and $\tilde{\boldsymbol{M}}_{di}$ become $(m_i + \bar{m}_i) \times (m_i + \bar{m}_i)$-dimensional matrices that are expressed as

$$\tilde{\boldsymbol{K}}_{di} \equiv \int_0^{a_i} E_i I_i \begin{bmatrix} \bar{\boldsymbol{S}}_i^z & \\ & \boldsymbol{O}_{\bar{m}_i} \end{bmatrix}^{\mathrm{T}} \begin{bmatrix} \bar{\boldsymbol{S}}_i^z & \\ & \boldsymbol{O}_{\bar{m}_i} \end{bmatrix} \mathrm{d}\bar{a}_{i+1} \tag{10e}$$

$$\tilde{\boldsymbol{M}}_{di} \equiv \int_0^{a_i} \rho_i \begin{bmatrix} \boldsymbol{S}_i^z & \\ & \boldsymbol{O}_{\bar{m}_i} \end{bmatrix}^{\mathrm{T}} \begin{bmatrix} \boldsymbol{S}_i^z & \\ & \boldsymbol{O}_{\bar{m}_i} \end{bmatrix} \mathrm{d}\bar{a}_{i+1} \tag{10f}$$

where $m_i \times m_i$-dimensional matrices $\bar{\boldsymbol{S}}_i^z$ and $\boldsymbol{S}_i^z$, are defined similar to (10d).

3.3 An illustration: a single flexible link

The method of determining structural damping coefficient, as presented in Sect. 3.2 above, is now illustrated using an example of a single flexible link. Only the vibrations in the link due to its flexibility characteristics are considered, without any joint motion imposed on the link, i.e., the flexible link is clamped at one end, as shown in Fig. 4. The beam is kept in such a way that it vibrates in horizontal plane. For the purpose of modeling, only first two modes are considered. Correspondingly, the determination of the structural damping coefficient in first two modes only is shown. For a single flexible link vibrating in its first two modes, equations of motion, (5), are expressed as

$$\rho\begin{bmatrix} \frac{a^3}{3}+k_{11}d_1^2+k_{12}d_2^2 & k_{21} & k_{22} \\ & k_{11} & \\ sym & & k_{12} \end{bmatrix}\begin{bmatrix} \ddot{\theta} \\ \ddot{d}_1 \\ \ddot{d}_2 \end{bmatrix}+\rho\begin{bmatrix} 2\dot{\theta}(k_{11}\dot{d}_1^2+k_{12}\dot{d}_2^2) \\ -k_{11}d_1\dot{\theta}^2 \\ -k_{12}d_2\dot{\theta}^2 \end{bmatrix}$$
$$=\begin{bmatrix} \tau_\theta \\ \tau_{d_1} \\ \tau_{d_2} \end{bmatrix}+\begin{bmatrix} 0 \\ \tau_{d_1}^s \\ \tau_{d_2}^s \end{bmatrix}+\begin{bmatrix} \kappa & 0 & 0 \\ & \zeta_1 & 0 \\ sym & & \zeta_2 \end{bmatrix}\begin{bmatrix} \dot{\theta} \\ \dot{d}_1 \\ \dot{d}_2 \end{bmatrix} \tag{11a}$$

Where ρ is the mass per unit length, a is the link length, θ is the joint angle, d_1 and d_2 are the generalized coordinates of the link vibrating in 1st and 2nd modes, respectively. Moreover, the terms, τ_θ, τ_{d_1}, and τ_{d_2} are respectively the generalized forces corresponding to the generalized coordinates, $\theta, d_{1,}$ and d_2. The terms, $\tau_{d_1}^s$ and $\tau_{d_2}^s$ are the terms due to strain energy [19, 21], whereas k_{1j} and k_{2j}, for $j = 1, 2$, are constants associated with the shape functions, i.e.,

$$k_{1j} \equiv \int_0^a s_{ij}^2\,\mathrm{d}\bar{a} \quad \text{and} \quad k_{2j} \equiv \int_0^a s_{ij}\,\mathrm{d}\bar{a} \tag{11b}$$

in which s_{ij} is the shape function of the link in j^{th} mode. Moreover, κ is the joint damping coefficient, and ζ_j, for $j = 1, 2$, is the associated structural damping coefficient of the link which will be determined here from the experimental data. The scheme of the experiment is shown in Fig. 4. Corresponding to the two modes of vibrations, the structural damping coefficients are given by, $\zeta_j = \xi_j\bar{\zeta}_j$, for $j = 1, 2$, in which $\tilde{\xi}_j$ and $\bar{\zeta}_j$ are respectively the structural damping ratio and critical damping factor associated with vibration in the j^{th} mode. The physical parameters of the link and the set-up are presented in Table 2. The physical dimensions and the mass properties of the link are so selected that the flexibility characteristics of the link are prominent. Moreover, the link is clamped horizontally and an accelerometer is mounted on its end, as indicated in Fig. 4. The output of the accelerometer is amplified using a charge amplifier and the readings are taken on a CRO. To determine the structural damping coefficients of the link, tip of the link is deflected by a known displacement (0.015 m) and released to vibrate in its natural condition. The amplitude decay curve of the link, as obtained from the accelerometer, is shown in Fig. 5(a). The structural damping coefficient, ζ_j, is then estimated by first determining the structural damping ratio $\tilde{\xi}_j$ using the method of evolving spectra explained in Sect. 3.2.1. A time window of 0.05 sec is selected. Two such positions of the time window, namely, the 1st and 4th, are shown in Fig. 5(a). FFT of the responses in different time windows are plotted to get Fig. 5(b). Figure 5(b) is called as the waterfall plot. For clarity of representation, FFT responses in only four locations of time window are shown. Since the peaks in the FFT curves are located corresponding to the natural frequencies of link, the amplitudes of the successive peaks on a particular natural frequency are now noted. Since the determination of structural damping coefficients is performed for the first and second modes, amplitudes of the successive peaks, namely, x_1 and x_2 for the 1st mode, as shown in Fig. 5(b), are noted. Then using (9c) the structural damping ratio $\tilde{\xi}_1$ is calculated. Similarly, the ratio for the 2nd mode, $\tilde{\xi}_2$, is obtained. Alternatively, the amplitude decay of the peaks of the FFT curves for the 1st and 2nd natural frequencies are plotted against time on a semi-logarithmic scale, as shown in Fig. 5(c). The slope of the curve divided by the corresponding natural frequency of the mode gives the

Table 2 Experiment with single flexible link (Fig. 4)

(a) Physical parameters of the link

Material	Length, a_i (m)	Cross-section (m^2)	Mass (kg)	Mass/length, ρ_i (kg/m)	Flexure stiffness $E_i I_i$ (N m^2)
Spring steel	0.33	0.024×0.001	0.060	0.1818	0.4

(b) Specifications of the equipments

Equipment	Specifications
Accelerometer, 2	20 g; Diapharm type
Charge amplifier, 3	Bruel and Kjaer, 2635;
	Lower frequency cut-off: 2 Hz;
	Higher frequency cut-off: 30 Hz;
	Calibration factor: 100 mV/mm;
	Charge sensitivity: 1.003 pC/ms^{-2};
	Voltage sensitivity: 0.88 mV/ms^{-2}
Data acquisition system, 4	Agilent, 54621oscilloscope; 60 MHz, 200 MSa/s

structural damping ratio for the particular mode at hand. For the link under study, the latter methodology, i.e., Fig. 5(c), is used, which results in $\tilde{\xi}_1 = 0.1980$ and $\tilde{\xi}_2 = 0.0428$. Next, the critical damping ratios, $\bar{\zeta}_j$, for $j = 1, 2$, are calculated using the link length a, the shape functions, and (10a)–(10f). The values are $\bar{\zeta}_1 = 6.9 \times 10^{-2}$ kg/s and $\bar{\zeta}_2 = 6.5 \times 10^{-3}$ kg/s. Finally, the structural damping coefficient, ζ_j, is obtained for $j = 1, 2$, using $\zeta_j = \tilde{\xi}_j \bar{\zeta}_j$, i.e., as $\zeta_1 = 1.37 \times 10^{-2}$ kg/s and $\zeta_2 = 2.8 \times 10^{-3}$ kg/s. These are then incorporated into (11). Next, the simulation is performed with the same initial conditions as that of Fig. 4. Simulation is done in Matlab v6.5, using ode45 solver which is based on the Runga–Kutta method. The DeNOC based recursive simulation algorithm presented in [4, 19] is adopted to calculate the joint accelerations, $\ddot{\boldsymbol{q}}$ from (5). The initial conditions are taken as follows: Since the tip of the link is initially deflected by a known amount, $\boldsymbol{u}$ which is given by [20],

$$\boldsymbol{u} \equiv \begin{bmatrix} \bar{s}_1^z & 0 \\ 0 & \bar{s}_2^z \end{bmatrix} \begin{bmatrix} d_1 \\ d_2 \end{bmatrix}$$

where, for $j = 1, 2$; $\bar{s}_j^z$ is the shape function associated with the bending of the link in j^{th} mode and evaluated at a, i.e., the tip of the link. These values are known and assuming $d_2 = 0$, d_1 is evaluated. Now, in order to use (11a) for the simulation, θ is always zero, i.e., $\theta = 0$ since one end of the link is clamped. Accordingly, $\dot{\theta} = \ddot{\theta} = 0$. Also, initially, $\dot{d}_1 = \dot{d}_2 = 0$. Simulation results for the tip-deflection of the link thus obtained are then compared with those obtained experimentally, as in Fig. 6. It is clear from the plots that the experimental and simulation results match closely, thus verifying the values for the structural damping coefficients as correct.

4 Experiments on simple robotic systems

In this section, a series of experiments conducted on simple robotic systems, including single flexible link and a two flexible links robotic arm are presented. The joint and structural

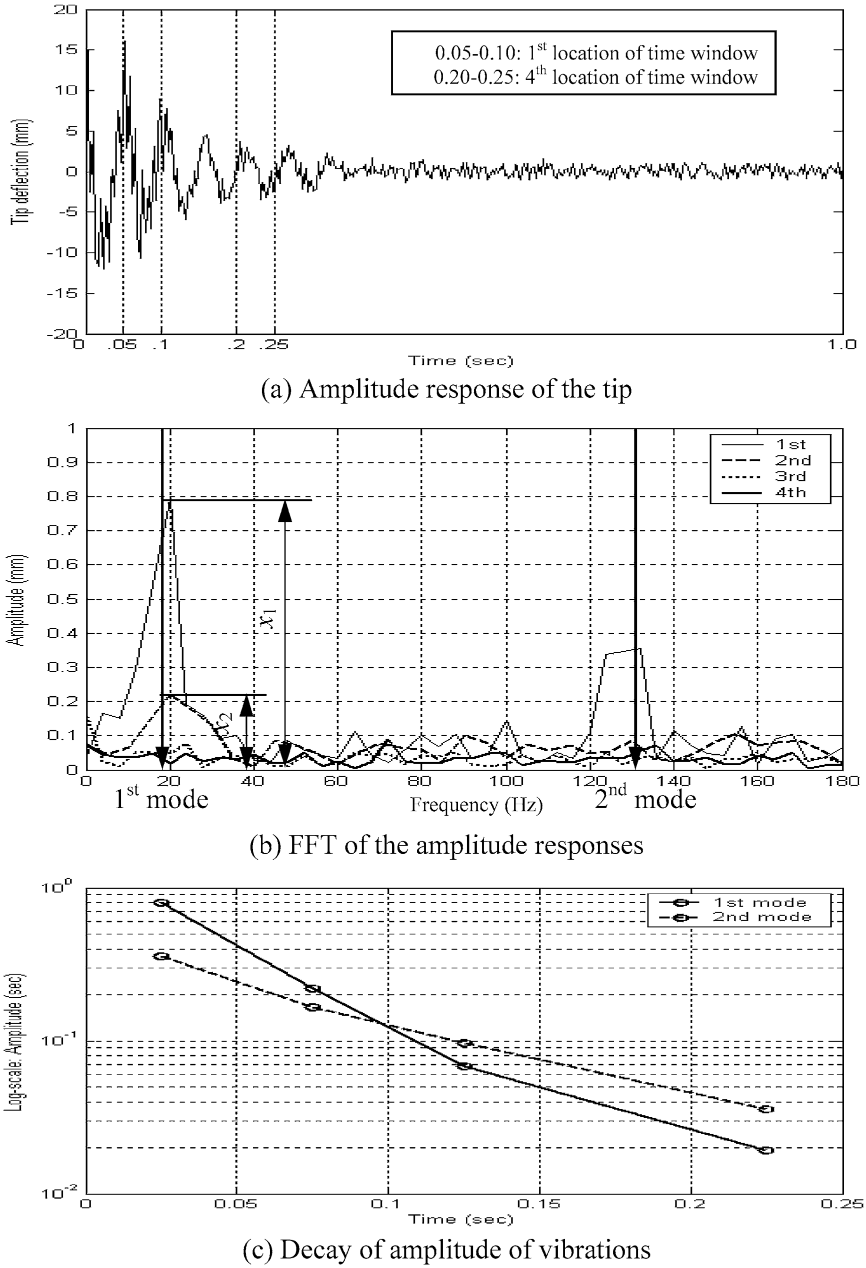

Fig. 5 Determination of structural damping ratio

damping coefficients of then determined using the methodology proposed in Sect. 3. The damping characteristics are then incorporated in the dynamic model given by (5). The simulation of the robotic systems is then carried on using the recursive, numerically stable forward dynamic algorithm proposed in [4, 19].

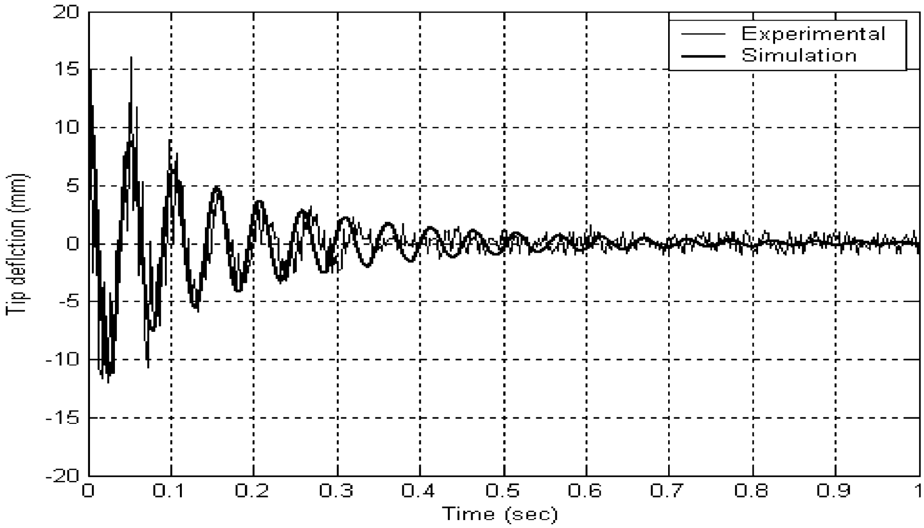

Fig. 6 Simulation results for clamped flexible link

4.1 Single flexible-link arm

In this section, results of the experiments conducted on a single flexible-link arm are reported. The flexible link used as moving arm is the same as used in Sect. 3.3. The fixed end conditions are replaced by a revolute joint and, the end-joint conditions are selected as fixed-free. The scheme of the experiment is shown in Fig. 7. The physical parameters of the link and the experimental set-up are shown in Table 3. The joint displacement of the link is measured using the potentiometer placed at the joint, whose inertia is included in the dynamic model as hub- inertia. The deflection at the tip of the link is measured using a full strain-gauge Wheatstone bridge mounted at the root of the link. Two strain gauges are mounted on each side of the link so that the proper conditioning of the readings is obtained giving the deflection direction correctly. The strain-gauge signals are amplified using an amplifier and the output is taken on the PICO CRO attached to the computer. The characteristic details of the equipments are shown in Table 3(b).

4.1.1 Calibration

In order to use the strain gauges to find the link deflection at its tip, it needs to be calibrated. First, the output of the strain-gauge bridge, i.e., the strain induced in the strain gauges due to the link bending, is recorded for a predetermined deflection of the link tip. Figure 8 shows the schematic set-up for this calibration, in which the link is clamped at one end, and its tip is deflected by putting known load on the load-cup. The deflection is measured using the dial gauge and corresponding change in the output voltage is recorded on a Sanwa DMM, PC5000digital multimeter of 0.01 Ω resistance and 0.01 mV resolution. Figure 9 shows the calibration curve for the strain-gauge bridge outputs. It can be seen that the bridge exhibits linear characteristics in the range of deflection, which is given by the equation written in Fig. 9 itself.

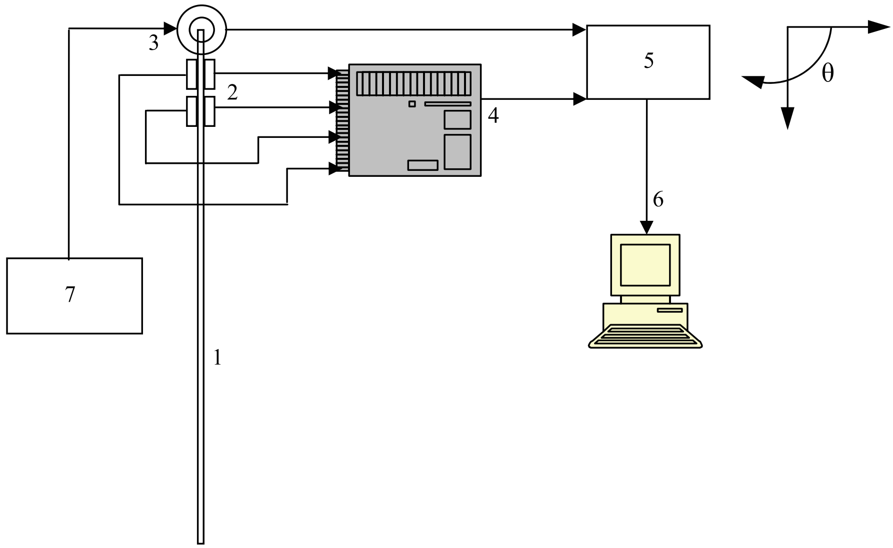

1. Flexible link; 2. Strain-gauges; 3. Potentiometer; 4. Amplifier; 5. PICO-CRO;

6. Computer; 7. Power supply

Fig. 7 Experimental set-up for single flexible-link arm

Table 3 Single flexible-link arm (Fig. 7)

(a) Physical parameters of the link

Material	Length, a (m)	Cross-section (m^2)	Mass (kg)	Mass/Length, ρ (kg/m)	Flexure stiffness, EI (N m^2)	Hub-inertia, I_h (kg m^2)
Spring steel	0.33	0.024×0.001	0.060	0.1818	0.4	2×10^{-5}

(b) Specifications of the equipments used

Equipment	Specifications
Amplifier, 4	ADAM-3016, DIN rail-mounted
Strain gauges, 2	350Ω, 100% gain
Computer, 6	3.5 GHz Pentium IV desktop PC
Potentiometer, 3	Same as Table 1(b)
Data acquisition system, 5 and 6	Same as Table 1(b)
Power Supply, 7	Same as Table 1(b)
Joint Bearings	Ball bearings (since the operating speeds and load are nominal and small)

4.1.2 Free-fall

In this subsection, results of the free-fall experiments with the single flexible-link arm are presented which are also compared with those obtained from the simulation results. To ob-

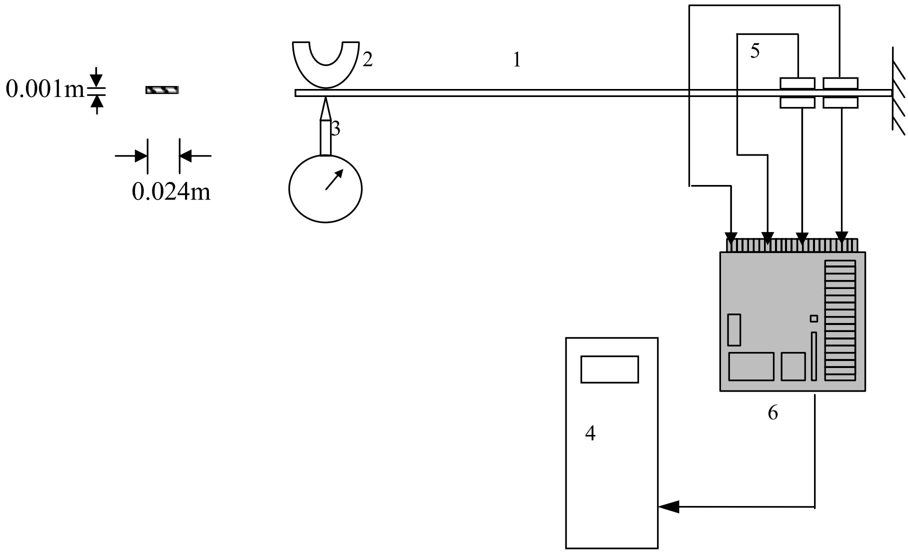

1. Flexible link; 2. Load-cup; 3. Dial-gage; 4. Multimeter; 5. Strain-gage bridge; 6. Amplifier

Fig. 8 Calibration of the strain-gauge bridge

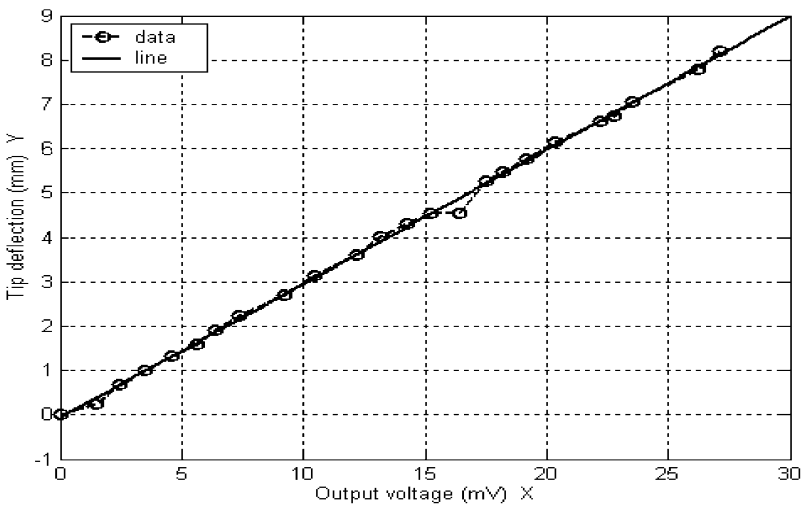

o: Reading points; y=0.3x-0.086

Fig. 9 Calibration curve for the strain-gauge bridge

tain the results, the link is allowed to fall freely under gravity from the horizontal position, as per Fig. 7, with no initial deflection and no external torque applied on it. The angular displacement of the joint was measured by the potentiometer, and the tip deflection of the link using the strain-gauges. The results are shown in Fig. 10(a, b). To compare the exper-

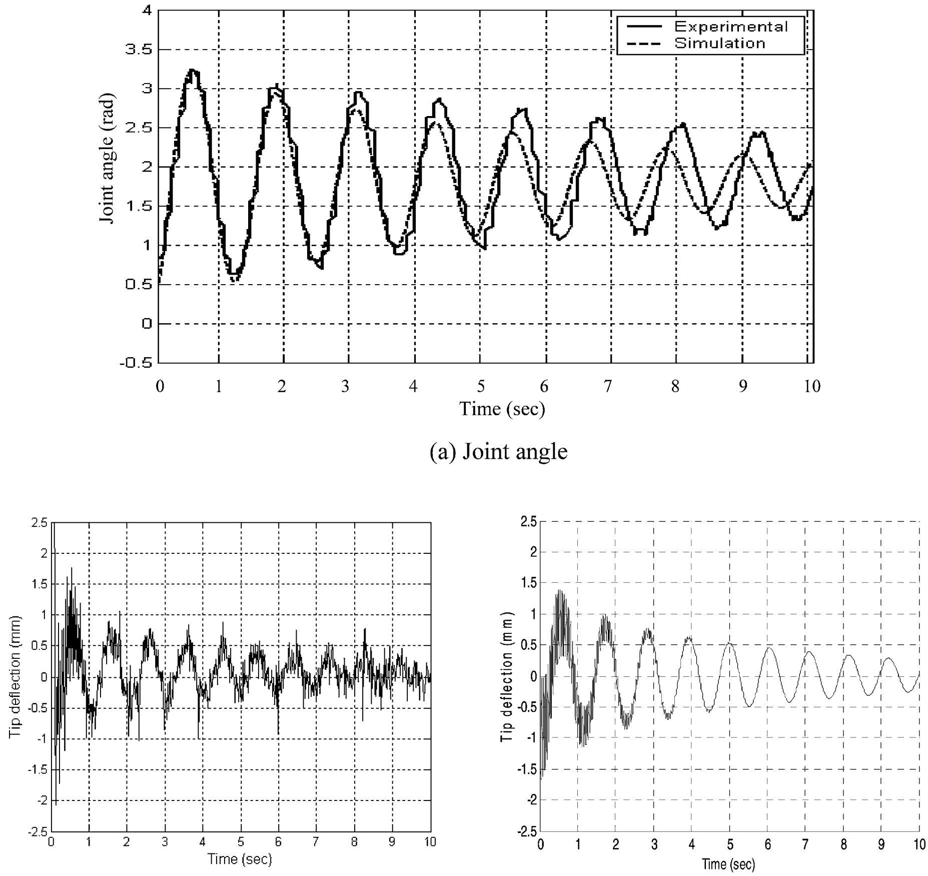

(a) Joint angle

Experimental

Simulation

(b) Tip deflection

Fig. 10 Free-fall results for the single flexible-link arm

imental results with those from the simulations, joint damping coefficient, and structural damping were first calculated respectively as $\kappa = 0.0106$ kg/s and $\zeta_1 = 1.37 \times 10^{-2}$ kg/s, $\zeta_2 = 2.8 \times 10^{-3}$ kg/s using the scheme presented in Sect. 3.2. The damping factors were then incorporated into (11a) and the free-fall simulation results were obtained using the proposed forward dynamics algorithm. Initially conditions for simulation were taken as, $\theta = d_1 = d_2 = 0$; $\dot{\theta} = \dot{d}_1 = \dot{d}_2 = 0$. Figures 10(a, b) show the comparisons of the experimental and simulation results for the joint angle and tip deflection of the link, respectively. The Fast Fourier Transformation, i.e., FFT, of the experimental results, Figs. 10(a, b) show an oscillation frequency of 1.1 Hz and the tip vibration frequency of 20.5 Hz, respectively. From the simulation results, the joint oscillation and tip vibration frequencies are 1.1 Hz is 21 Hz, respectively. Also, the amplitudes of joint oscillations and tip vibrations also match closely, particularly during the first three–four cycles. The mismatch in the peak height values is attributed to the fact that the real beam vibrates in all possible modes of vibration, whereas the simulation considered only for first two modes of vibration. The worsening of

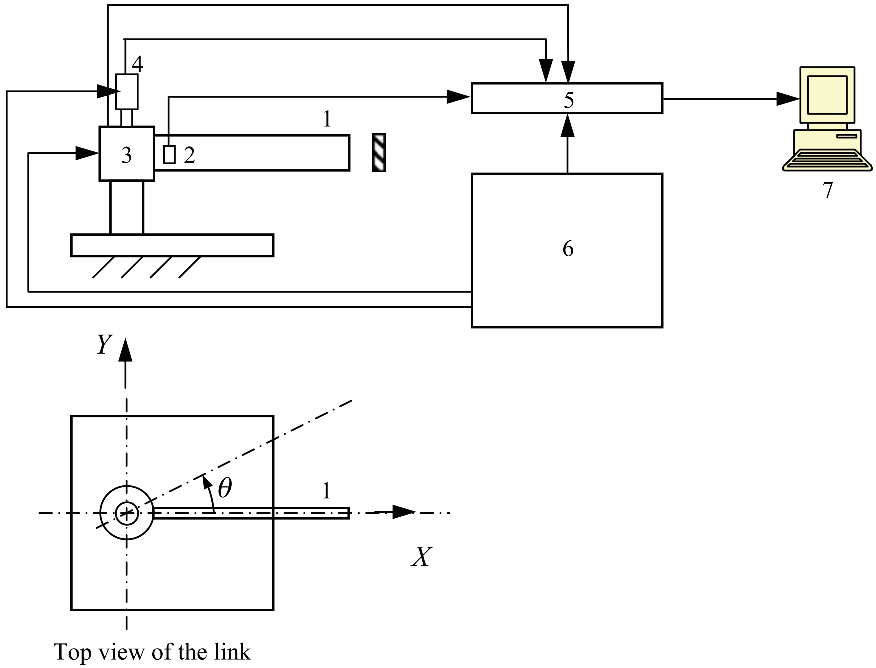

1. Flexible link; 2. Load-cell; 3. Servomotor and potentiometer Assembly; 4. Torque sensor; 5. PICO CRO; 6. Power supply; 7. Computer

Fig. 11 Set-up for the forced experiment with single flexible-link arm

results in the latter part is mainly due to linear decay considerations of the damping factors given by (10).

4.1.3 Forced response

In this subsection, the same arm, as considered in the previous subsection, was subjected to a specified torque excitation at its joint. For this, the experimental set-up is shown in Fig. 11. The specifications of the set-up are shown in Table 4. The torque is applied on the link by the servomotor. Torque specification of the servomotor is 0.011 N m. However, note that, the torque generated by the servomotor depends on the load applied and varies along the rotation of robotic link. Actually, in order to get the desired accuracy in the simulation results, it is essential to determine the actual torque applied by the servomotor on the link. Note that, a servomotor can be run in two modes, namely, (i) constant speed; and (ii) constant torque. Although, for the experimental set-up described in this paper, it is desired to have constant torque characteristics, it will be difficult to measure the variation in actual speeds that come along with constant torque mode of operation. Moreover, it is not possible to maintain the positional accuracy of the servo if the drives are operated for constant torque characteristics. It is, on the other hand, viable to measure the variation in output torque of the servomotor as applied on the beam. The variation in the torque output of the servomotor and applied on the beam is measured using a torque sensor. Consequently, a reaction rotary torque transducer is mounted on the servo. The selection of a reaction torque sensor is based on its advantage that

Table 4 Set-up for the forced experiment with single flexible-link arm (Fig. 11)

(a) Physical parameters of the link, 1

Material	Length, a (m)	Cross section (m^2)	Mass (kg)	Mass/length, ρ (kg/m)	Flexure rigidity EI (N m^2)	Hub-inertia (kg m^2)
Spring steel	0.33	0.024×0.001	0.060	0.1818	0.4	7×10^{-5}

(b) Specifications of the equipments

Equipment	Specifications
Actuator, 3	M5945G-11 Standard Delux digital coreless servomotor operating voltage range: 4.8–6.0 V
Potentiometer, 3	Wire-wound
Load-cell, 2	350 Ω, activation voltage 5 V
Data acquisition system, 4 and 5	Same as Table 1(b)
Torque sensor	Honeywell; QWLC-8M, BT311 Miniature; Bonded foil strain gage type
Power Supply, 6	Same as Table 1(b)
Joint Bearings	Ball bearings
Transmittion chain	Geared output of servomotors linked at the joints through ball bearings

it minimizes the error attributable to the inertia of rotating components. The specification details of the torque sensor are given in Table 4(b). The control system on the servomotor is designed such that the motor applies its maximum torque (0.011 N m) while moving the link from any random initial position to the reference position of the set-up. Moreover, as soon as the link reaches its final position, which is the reference position of link for the control circuit, motor stops applying torque and brakes are applied on the link to bring it to the rest. The angular rotation of the link is measured using the potentiometer mounted on the servomotor. The deflection of the link is measured using two load-cells, one mounted on each side of the link. The output of the load-cells, torque sensor, and the potentiometer are taken on a CRO having interface with the computer.

To generate the experimental results, first, the output of the load-cells bridge was calibrated. To do this, the link was locked at its joint and a known deflection in the lateral direction was imparted at the other end of the link. The output of the load-cells bridge for the given deflection was recorded. The process is repeated by changing the deflection of the link. Finally, to obtain the calibration curve for the load-cells the link deflections are plotted against the output voltages, as shown in Fig. 12(a). A series of experiments were then conducted for different initial angular displacements, namely, $\theta = -80°, -60°, -40°$, as per Fig. 11. In order to obtain the value of input torque for simulation algorithms, the output the torque sensors were recorded to get the real time values of the torque applied on the beam along its rotational trajectory, as shown in Fig. 12(b). Then using the cubic-spline interpolation in Matlab v6.0 a shape preserving curve is fitted on it as shown in Fig. 12(b). The cubic spline curve function is then given as input in the simulation algorithm. Simulation results with initial conditions $\theta = -40°, d_1 = d_2 = 0; \dot{\theta} = \dot{d}_1 = \dot{d}_2 = 0$ are then obtained after incorporating the experimentally obtained real time torque values, joint, and structural damping as mentioned above. The comparison of the results is shown in Figs. 13(a, b). Note

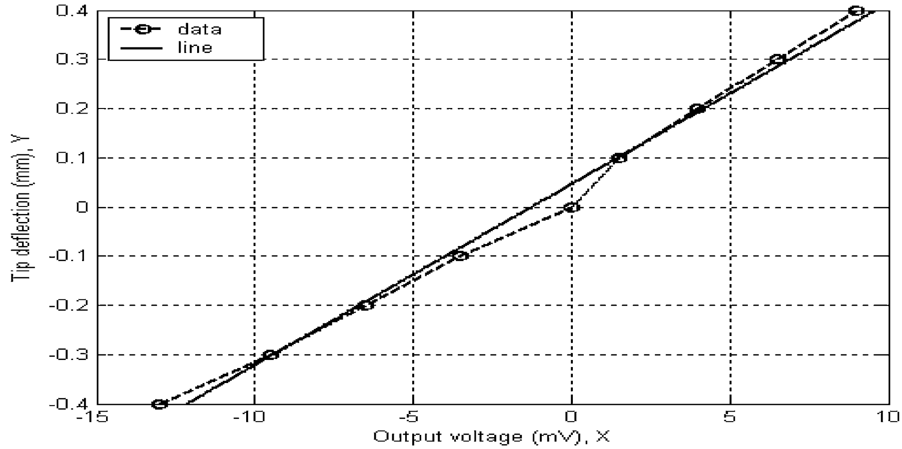

o: Reading points; y=0.037x+0.04

(a) Calibration of load cells for known values of deflection

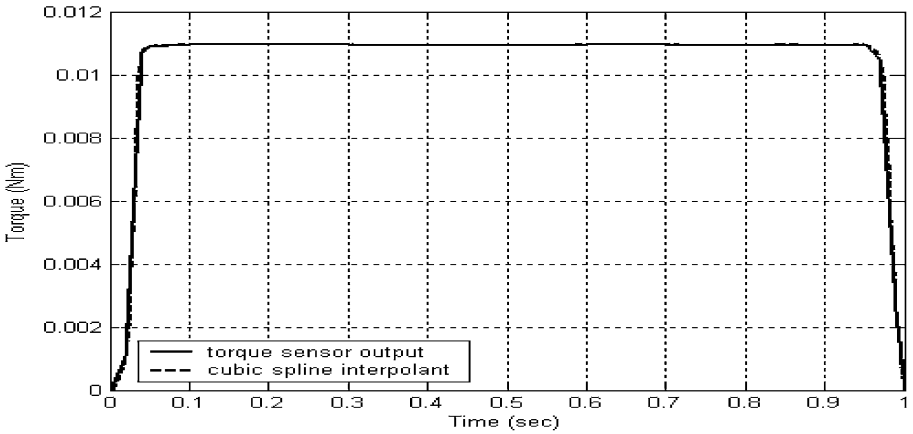

(b) Torque applied at the flexible link: Calibrated values of torque sensor and its equation using cubic spline fitting interpolation for input in simulation

Fig. 12 Deflection (load cells) and torque (torque sensor) calibration: forced response of the single flexible-link

that, the inertial and dynamic effects of potentiometer, servomotor, and torque transducer are included suitably in the simulation model as the hub inertia.

The results corresponding to other initial conditions are similar, and hence not reported. Since the end conditions of the link remains same as those in Sect. 3.3, same structural damping coefficients, i.e., $\zeta_1 = 1.37 \times 10^{-2}$ kg/s, $\zeta_2 = 2.8 \times 10^{-3}$ kg/s, were taken. A comparison of the simulation and experimental results for the joint angles, Fig. 13(a), and the tip deflections, Fig. 13(b), show that the results are matching. Thus, for example, the frequency of vibrations of the tip of the link obtained from the experimental results is 21.75 Hz, whereas the same from the simulation results is 21.5 Hz, which are close. The amplitude of vibrations are also closely matching, as seen in Fig. 13(b).

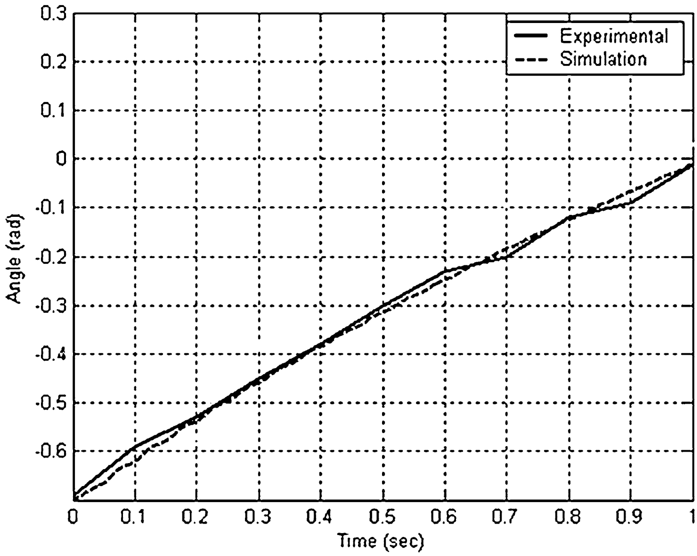

o: Reading points; y=0.037x+0.04

(a) Joint angle

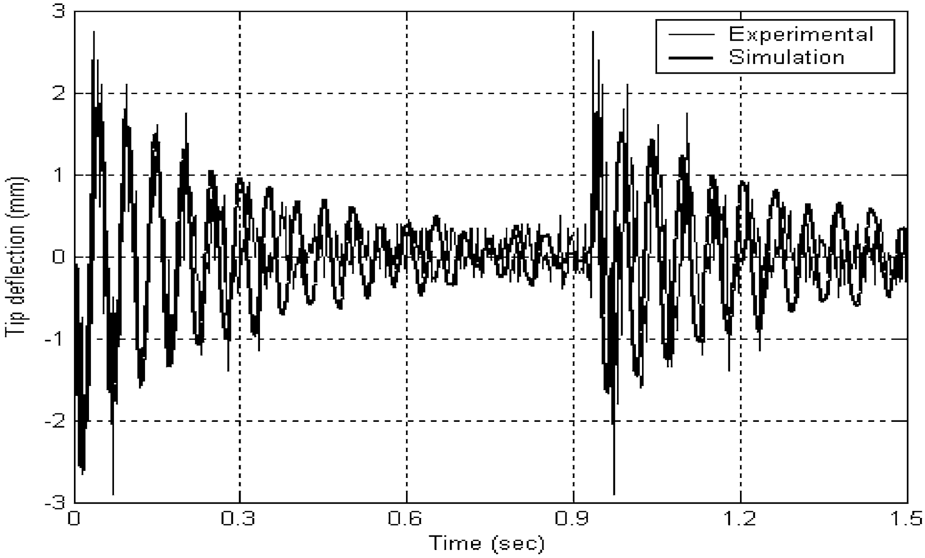

(b) Tip deflection

Fig. 13 Forced response of the single flexible-link arm

4.2 Two flexible-link robotic arm

In the previous section, a comprehensive experimental validation of the proposed dynamic modeling for a flexible link under different conditions has been presented. In this section, an experimental validation of the proposed dynamic modeling for a two flexible-link robotic

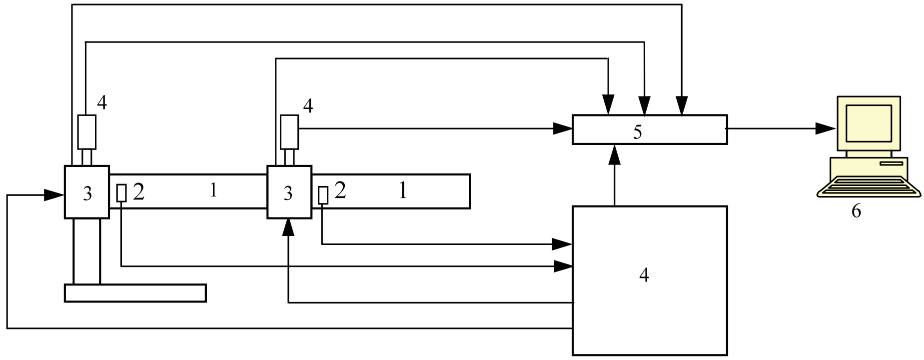

1. Two flexible-links; 2. Load cells; 3. Servomotor and pot; 4. Torque Sensor;

5. Pico CRO; 6. Power supply and amplifier; 7.Computer

Fig. 14 Set-up for the forced experiments with two-flexible-links robotic arm

Table 5 Physical parameters of the links

I	Material	Length, a_i (m)	Cross section (m^2)	Mass (kg)	Mass/length, ρ_i (kg/m)	Hub Inertia (kg m^2)	Flexure rigidity, $E_i I_i$ (N m^2)	Payload (kg)
1	Spring steel	0.24	0.024×0.0005	0.020	0.0833	5×10^{-5}	0.05	0.210
2	Spring steel	0.19	0.024×0.0005	0.017	0.1053	5×10^{-5}	0.05	0

arm, is presented. The two flexible-link robotic arm represents a system of multiple flexible links coupled together. Hence, the main objective behind presenting the experimental results and their comparison with the simulation results for a two flexible-link robotic arm is to validate the model for a representative serial multiple-link robot. Moreover, the methodology for the estimation of damping and its incorporation in the dynamic model is also tested for a multiple flexible link robot. The schematic diagram of the experimental set-up for conducting the experiments on two flexible-link arm is shown in Fig. 14. Characteristic details of the equipments used are shown in Table 4(b) The joint bearings and transmittion types are also given in Table 4(b). whereas the physical parameters of the links are shown in Table 5.

Like forced single flexible-link arm experiments, torque is applied by the servomotors at the two joints. Torque sensors are mounted on each servo motor to obtain the real time value of torque applied on each beam during the experiments. For the simulation, the effect of servomotors, Potentiometers, torque sensors, and the joint fixtures at each joint is taken into account as hub inertias on the link. Moreover, for the purpose of obtaining the experimental results, the potentiometer and load-cell at each joint are calibrated, as plotted in Fig. 15(a, b). The characteristics of the potentiometer and the load-cells are linear, as seen in Fig. 15(a, b). The torque sensor readings are used to generate the spline torque function to be given as input to the simulation algorithms. This is similar to the strategy adopted for forced experiments on single flexible link systems. The forced response of the arm is then obtained by applying a torques as shown in Fig. 16(a, b) for each link. Note that the maximum value of torque applied is 0.011 N m on the 1st joint and 0.007 N m on

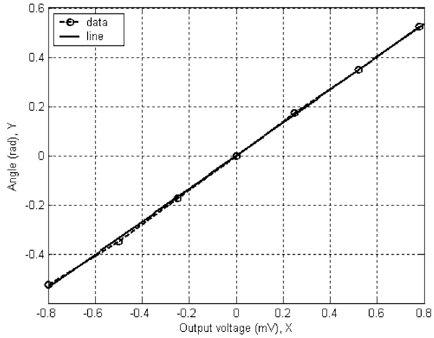

o: Reading points; y=0.02x+0.013

Joint 1

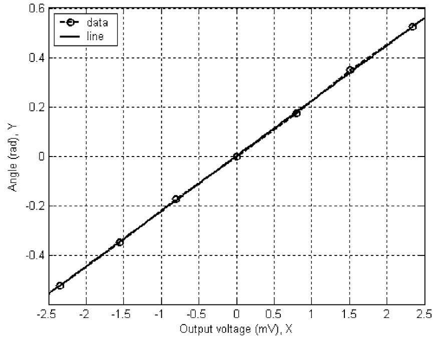

o: Reading points; y=0.025x+0.01

Joint 2

(a) Calibration curves for pots

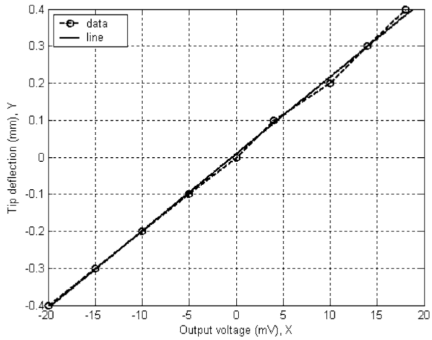

o: Reading points; y=0.02x+0.013

Joint 1

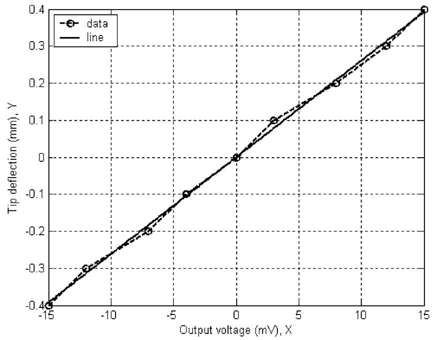

o: Reading points; y=0.025x+0.01

Joint 2

(b) Calibration curves for load cells

Fig. 15 Deflection (load cells), and potentiometer (Pot) calibration: forced response of the two-flexible link robotic arm

the 2nd joint. A series of experiments, determining the forced responses of the arms, for different initial configurations of the arm, namely, $\theta_1 = -80°, \theta_2 = 80°$; $\theta_1 = -60°, \theta_2 = 60°$, and $\theta_1 = -40°, \theta_2 = 40°$ were obtained. The results are compared for $\theta_1 = -40°, \theta_2 = 40°$ with the simulation results, as shown in Figs. 17(a, b). Behaviors for other initial conditions are similar. The joint angles were measured with the potentiometers, readings of the torques were taken using the torque transducers, and the deflections were measured with the load-cells. Note that the determination of real time torque values for both the beams was done using the methodology presented in Sect. 4.1.3 wherein, the output of the torque sensors is recorded to get the real time values of the torque applied on the beam and using the cubic-spline interpolation in Matlab v6.0 a shape preserving curve is fitted on it. The cubic spline curve function is then given as input in the simulation algorithm. Figure 16(a, b) show the real time torque values for 1st and 2nd links as obtained from the respective torque sensors. The determination of the damping was done based on the methodology presented in Sect. 3.2 whose plots are shown in Fig. 18. The corresponding values are, $\zeta_{11} = 0.0922$ kg/s, $\zeta_{12} = 0.0708$ kg/s, $\zeta_{21} = 0.0807$‘kg/s, and $\zeta_{22} = 0.1348$ kg/s. Again, for simulation only, the

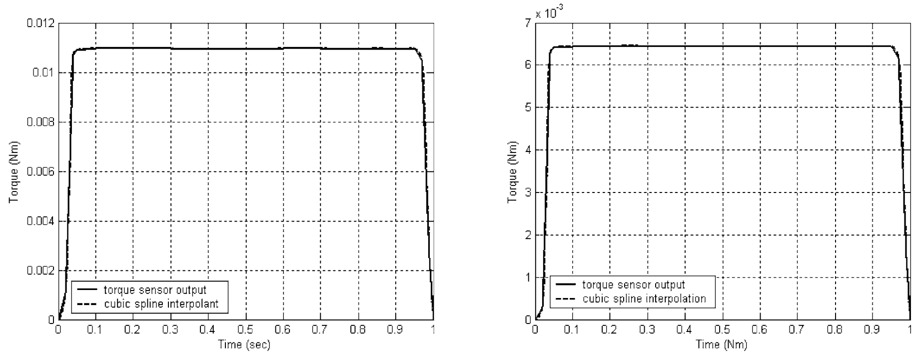

link 1: inner link link2: outer link

Fig. 16 Torque applied at the flexible link of two flexible links robotic system: calibrated values of torque sensor and its equation using cubic spline fitting interpolation for input in simulation

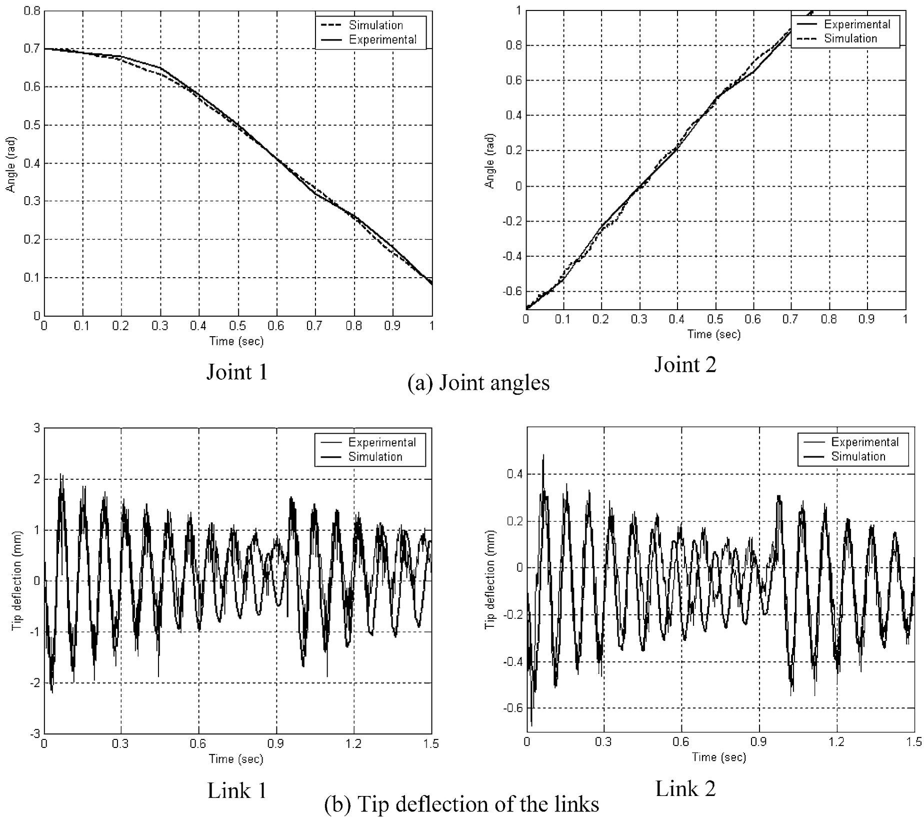

Fig. 17 Results for two flexible-link robotic arm

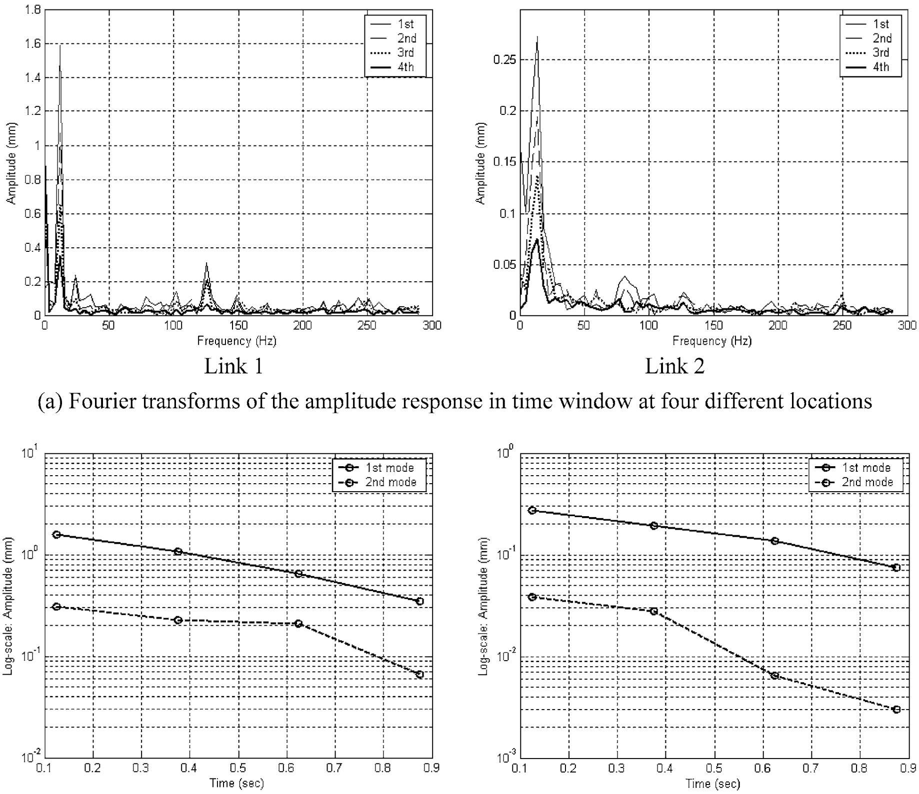

Link 1 Link 2

(a) Fourier transforms of the amplitude response in time window at four different locations

Link 1 Link 2

(b) Decay of amplitude of vibrations corresponding to 1st and 2nd modes

Fig. 18 Determination of structural damping ratios for two flexible-links arm

first two modes were considered for the vibration of each link. Since the link is brought to rest through the feed-back control systems of the servomotors, the natural joint damping coefficients were taken as zeros, i.e., $\kappa_1 = \kappa_2 = 0$. Initial conditions for the simulation were taken as, $\theta_1 = -40°, \theta_2 = 40°$, and for $i = 1, 2, d_{i1} = d_{i2} = 0; \dot{\theta}_1 = \dot{\theta}_2 = \dot{d}_{i1} = \dot{d}_{i2} = 0$.

Similar to strategy adopted for single link experiments, the inertial and dynamic effects of potentiometer, servomotor, and torque transducer are included suitably in the simulation model as the hub inertia.

The simulation results for the joint angle variations and the tip deflections are shown in Figs. 17(a, b), which are compared with those obtained experimentally. The results for the joint angles are matching closely. Similarly, the tip deflection results, are also matching closely. Thus, for example, the frequency of vibrations of the tip of the first link obtained from the experimental results is 11.75 Hz, whereas the same from the simulation results is 11.5 Hz, which are close. For link 2, the frequencies of tip vibrations from the experiment and simulation are 13.5 Hz and 13.0 Hz, respectively. The amplitude of vibrations are also closely matching, as seen in Fig. 17(b).

5 Conclusions

Dynamic modeling of rigid-flexible links, incorporating the effects of damping, and a methodology for the estimation of various damping coefficients is presented. The dynamic modeling is done using the DeNOC matrices. Verification of the proposed dynamic model and experimental procedure for estimation of damping coefficients is done using a series of experiments conducted on simple robotic systems. Joint damping coefficients are measured using the logarithmic decay characteristics, while the structural damping coefficients are estimated using the modal analysis and method of evolving spectra. In fact, the application of method of evolving spectra, also called the Waterfall method; to extract information about the structural damping coefficients is one of the original contributions of this paper. The advantages of the proposed method of determination of structural damping are that besides being simple and accurate, it also provides information about the time-based amplitude response of the vibration in each mode. This information is of vital importance in designing the feedback control system for the flexible links. Moreover, by using the proposed method, an estimate of structural damping coefficients in each individual mode of vibrations of flexible links is obtained. Note that most of the experimental methods available in literature provide information about overall structural damping coefficient of the system and not the damping coefficients of vibrations of flexible links in each of its individual modes. Using the proposed methodology and procedure, the structural damping coefficients of the flexible links in each of the individual modes of vibrations are obtained separately. Such information is important for accurate, efficient, and real-time control algorithms. Furthermore, the method is based on the FFT of the vibration responses; hence, the effects of noise are also filtered out from the experimental data. Another feature of the methodology presented here is that it is based on the Decoupled Natural Orthogonal (DeNOC) matrices for the flexible links using which the matrices for vibration amplitude propagation are decoupled from the twist propagation matrices. In addition, recursive formulation of simulation algorithms and better physical interpretation of many terms is made possible. Using the proposed methodology and procedure, it is possible to decouple the flexible twist propagation and the joint-cum amplitude propagation along the links of serial robotic systems with rigid and flexible links. Moreover, using the proposed method, the structural damping coefficients of the flexible links in each of the individual modes of vibrations are obtained separately. Such information is important for accurate, efficient, and real-time control algorithms. Later in the paper, experiments on a commercially built two flexible-link robotic arm are explained and the results for the joint displacements and tip deflections are presented. Moreover, note that the exact torque applied at the joints is estimated using the torque transducers and spline fitting technique, and this value of torque is then given as input in the simulation. Furthermore, the hub-inertia at the joint of each motors, which is due to the servomotors, potentiometers, and the torque sensors along with assembly are modeled accurately and included in simulation algorithm. Thus,, the simulation algorithm accurately incorporates the various parameters in conducted experiments.

Acknowledgement The research work reported in this paper is carried out under the partial financial aid from the DST, Government of India (SR/S3/RM/46/2002) which is duly acknowledged.

References

1. Cyril, X.: Dynamics of flexible link manipulators. Ph.D. dissertation, McGill University, Canada (1988).

2. De Luca, A., Siciliano, B.: Closed-form dynamic model of planar multilink lightweight robots. IEEE Trans. Systems. Man Cybern **21**(4), 826–838 (1991)
3. Martins, J., Botto, M.A., Da Costa, J.: Modeling of flexible beams for robotic manipulators. Multibody Syst. Dyn. **7**, 79–100 (2002)
4. Mohan, A., Saha, S.K.: A recursive, numerically stable, and efficients simulation algorithm for serial robots with flexible links. Multibody Syst. Dyn. (2008). doi:10.1007/s11044-008-9122-6
5. Lankarani, H.M., Nikravesh, P.E.: A contact force model with hysteresis damping for impact analysis of multibody systems. ASME J. Mech. Des. **112**, 369–376 (1990)
6. Ambrosio, J.A.C., Rayn, P.: Elastodynamics of multibody systems using generalized inertial coordinates and structural damping. J. Mech. Struct. Mech. **25**(2), 201–219 (1997)
7. Austin, E.M., Inman, D.J.: Errors in damping predictions due to kinematic assumptions for sandwich beams. In: Proc. of Int. Conf. on Structural Dynamics–Recent Advances, pp. 515–526 (2000)
8. Mingli, B., Zhou, D.H., Schwarz, H.: Identification of generalized friction for experimental planar two-link flexible manipulator using strong tracking filter. IEEE Trans. Robot. Autom. **15**(2), 362–369 (1999)
9. Chapnik, B.V., Heppler, G.R., Aplevich, J.D.: Modeling impact on a one link-flexible robotic arm. IEEE Trans. Robot. Autom. **7**(4), 479–488 (1991)
10. Feliu, V., Garcia, A., Somolinos, J.A.: Gauge-based tip position control of a new three degree of freedom flexible robot. Int. J. Robot. Res. **20**(8), 660–675 (2000)
11. Mavroidis, C., Dubowsky, S., Raju, V.: End-point control of long reach manipulator systems. In: Proc. of IX World congress on Theory of Machines and Mechanisms, Milan, Sept 1–3 (1995)
12. Stieber, M.E., McKay, M., Vukovich, G., Petriu, E.: Vision based sensing and control for robotics applications. IEEE Trans. Instrum. Meas. **48**(4), 807–812 (1999)
13. De Luca, A., Siciliano, B.: Regulation of flexible arms under gravity. IEEE Trans. Robot. Autom. **9**(4), 463–467 (1993)
14. Bragliato, B., Rey, D., Pastore, J., Barnier, J.: Experimental comparison of nonlinear controllers for flexible joint manipulators. Int. J. Robot. Res. **17**(3), 260–281 (1998)
15. Queiroz, M.S., Donepudi, S., Burg, T., Dawson, D.M.: Adaptive nonlinear boundary control of a flexible link robot arm. IEEE Trans. Robot. Autom. **15**(4), 779–787 (1999)
16. Feliu, J., Feliu, V., Cerrada, C.: Load adaptive control of single-link flexible arms based on a new modeling technique. IEEE Trans. Robot. Autom. **15**(5), 793–814 (1999)
17. Stanway, J., Sharf, I., Damaren, C.: Validation of a dynamics simulation for a structurally flexible manipulator. In: Proc. of IEEE Conf. on Robotics and Automation, Minnesota, pp. 1959–1964 (1996)
18. Nikravesh, P.E.: Computer-Aided Analysis of Mechanical Systems. Prentice Hall, New Jersey (1988)
19. Mohan, A.: Dynamic analysis of flexible multibody robotic systems, Ph.D. dissertation, IIT Delhi, Delhi (2006)
20. Meirovitch, L.: Analytical Methods in Vibrations. Macmillan, New York (1967)
21. McIntyre, M.E., Woodhouse, J.: On measuring the elastic and damping constant of orthotropic sheet materials. Acta Metal. **36**(6), 1137–1416 (1988)
22. Thompson, W.T.: Theory of Vibration with Applications. Prentice Hall, London (1988)
23. Andersson, S., Söderberg, A., Stefan, B.: Friction models for sliding dry, boundary and mixed lubricated contacts. Tribol. Int. J **40**, 580–587 (2007)
24. Pazdera, I.: Friction models in servodrives. Available online, http://www.feec.vutbr.cz/EEICT/2007/sbornik/03-doktorske_projekty/04-silnoprouda_elektrotechnika_a_elektroenergetika/14-xpazde05.pdf
25. Canudas de Wit, C., Olsson, H., Åström, K.J., Lischinsky, P.: A new model for control of systems with friction. IEEE Trans Autom. Control **40**(3), 19–25 (1995)
26. Jonker, J.B., Aarts, R.G.K.M., Waiboer, R.R.: Modelling of joint friction in robotic manipulators with gear transmissions. In: Garcia Orden, J.C., Goicolea, J.M., Cuadrado, J. (eds.) Multibody Dynamics—Computational Methods and Applications. Computational Methods in Applied Sciences, vol. 4, pp. 221–243. Springer, Berlin (2007). 978-1-4020-5683-3
27. Norito, N., Shigeru, A.: Evaluation of amplitude dependence of internal friction in high-damping metals. Nippon Kinzoku Gakkaishi **65**(2), 109–114 (2001)
28. De Morton, M.E., Lott, S.A., Stainsby, D.F.: Measurement of internal friction by velocity observations of torsional oscillations. J. Sci. Instrum. **40**, 441–443 (1963)
29. Matveev, V.V.: On determining the damping properties of systems with amplitude-dependent resistance. J. Strength Mater. **2**(5), 407–413 (1973)
30. Wang, Y.Z., Ding, X.D., Xiong, X.M., Zhang, J.X.: Comparative analysis of internal friction and natural frequency measured by free decay and forced vibration. Rev. Sci. Instrum. **78** (2007)